

# Angular Dependence of the Ion-Induced Secondary Electron Emission for He<sup>+</sup> and Ga<sup>+</sup> Beams

Vincenzo Castaldo,<sup>1\*</sup> Josephus Withagen,<sup>1</sup> Cornelius Hagen,<sup>1</sup> Pieter Kruit,<sup>1</sup> and Emile van Veldhoven<sup>2</sup>

<sup>1</sup>Department of Applied Science, Delft University of Technology, Lorentzweg 1, Delft, Zuid-holland 2628CJ, The Netherlands

<sup>2</sup>TNO Science and Industry, Stieltjesweg 1, Delft, Zuid-holland 2628CK, The Netherlands

**Abstract:** In recent years, novel ion sources have been designed and developed that have enabled focused ion beam machines to go beyond their use as nano-fabrication tools. Secondary electrons are usually taken to form images, for their yield is high and strongly dependent on the surface characteristics, in terms of chemical composition and topography. In particular, the secondary electron yield varies characteristically with the angle formed by the beam and the direction normal to the sample surface in the point of impact. Knowledge of this dependence, for different ion/atom pairs, is thus the first step toward a complete understanding of the contrast mechanism in scanning ion microscopy. In this article, experimentally obtained ion-induced secondary electron yields as a function of the incidence angle of the beam on flat surfaces of Al and Cr are reported, for usual conditions in Ga<sup>+</sup> and He<sup>+</sup> microscopes. The curves have been compared with models and simulations, showing a good agreement for most of the angle range; deviations from the expected behavior are addressed and explanations are suggested. It appears that the maximum value of the ion-induced secondary electron yield is very similar in all the studied cases; the yield range, however, is consistently larger for helium than for gallium, which partially explains the enhanced topographical contrast of helium microscopes over the gallium focused ion beams.

**Key words:** FIB, secondary emission, angular dependency, image formation, He microscope

## INTRODUCTION

For years, the only ion sources used in focused ion beams (FIBs) have been the liquid metal ion sources (Seliger et al., 1979), especially the ones employing gallium ions. Since gallium (and in general, metallic) ions are heavy, the amount of energy and momentum that they transfer to the sample is destructive for the sample itself; this effect (sputtering) has prevented the FIBs from being used as microscopes and limited them to employment as nano-fabrication tools (Orloff, 1993; Orloff et al., 2003). Ga-induced secondary electron images were only used to find the sputtering and/or the redeposition target and inspect the results. In the last decade, however, considerable effort has been devoted to the design and development of novel ion sources, employing gaseous light ion species, such as helium, which gave renewed attention to FIBs as microscopes [scanning ion microscopes (SIMs)]. They now compete with, and complement, the traditional scanning electron microscopes (SEMs) in terms of brightness, current, spot size, and, ultimately, imaging resolution (Tondare, 2005).

The use of ions instead of electrons in scanning microscopy has some undiscussed advantages, such as different contrast mechanisms, smaller spot size, and perhaps higher resolution, also due to the much smaller wavelength (Ishitani & Ohya, 2003; Ohya & Ishitani, 2003). The gas field ion sources, in particular, provide high current in a sub-

nanometer spot (i.e., high brightness) and very low aperture angle at the sample, resulting in high depth of focus (Ward et al., 2006; Hill et al., 2008). The contrast mechanism most frequently used is the collection of secondary electrons (SEs), for they are produced in a much larger amount than other species (like backscattered ions that can also be used to form images) (Bell, 2009; Ogawa et al., 2010). It is common practice, in literature, to refer to ion-induced secondary electrons and electron-induced secondary electrons with iSE and eSE, respectively. A good way to estimate the imaging capability of an ion imaging machine is thus to measure, and/or simulate, the iSE yield ( $\delta_i$ , the number of secondary electrons per incident ion) as a function of the angle  $\alpha$  formed between the incident beam and the surface. These curves are responsible for the “first order contrast,” while other effects, such as edge enhancement and transparencies, can only be explained in terms of ion/atom interaction at the atomic level in a finite volume inside the sample (interaction volume). However, ions are always much more massive than electrons, and the sputtering, with consequent sample modification, is an ever-present unwanted effect, even with He ions. It has been shown that the removal of sample atoms is in fact the mechanism that ultimately limits the resolution of SIMs (Orloff et al., 1996; Castaldo et al., 2008, 2009).

The objective of this study is the measurement of  $\delta_i$  as a function of the angle  $\alpha$ . Curves for 25 keV He<sup>+</sup> beams and 30 keV Ga<sup>+</sup> beams incident on Al and Cr samples are presented and discussed.

## ANGULAR DEPENDENCE OF ION-INDUCED SECONDARY ELECTRON EMISSION

When energetic ions impact on a solid surface, they slow down in a pseudo-continuous process of energy loss. Eventually, they can find their way out from the top surface of the sample (backscattered ions), or from its bottom, if the sample is thin enough (transmitted ions), but most of the time their energy drops to a level that does not allow any further movement and the ions end up in a rest position in the target. In any case, due to the energy transfer from the beam, many secondary processes take place in the target: emission of photons, emission of electrons (SEs), emission of ions, displacement of target atoms (with consequent creation of point defects in crystals), sputtering of target atoms, nuclear reactions, and chemical reactions (creation and breaking of molecular bonds). Secondary emission is the process that is mostly used in image formation. It can be further divided into *secondary ion emission*, occurring when surface atoms are ionized and expelled, and *secondary electron emission*, occurring when shell electrons receive enough energy to reach the surface and overcome the surface energy barrier (SEB). Since in most cases SEs are the species produced in the largest amount, they are most commonly used to create an image. Secondary electron emission is the process that will be addressed here. Furthermore, the amount of secondary emission is very surface sensitive, thus providing good topographical (and, in some cases, material) contrast.

Ion-induced electron emission is in general due to two different processes, one of which can be dominant, depending on the ion species and energy.

### Potential Emission

This might occur when the potential energy of the ion is twice or more the work function of the solid and takes place in front of the solid surface: SE emission proceeds via resonance neutralization and subsequent Auger de-excitation or Auger neutralization (Hagstrum, 1954a, 1954b). It does not play a role in the case of  $\text{Ga}^+$  bombardment because the ionization potential for gallium is  $\sim 6$  eV, and for normal metals  $\Phi \sim 4\text{--}5$  eV, while for helium, whose first ionization potential is  $\sim 24.6$  eV, potential emission could be present. This process, however, becomes important only for slow ions and/or at grazing incidence, but it is usually negligible under standard scanning ion imaging conditions, where primary energies are in the order of tens of keV (Ramachandra et al., 2009).

### Kinetic Emission

This occurs for direct transfer of kinetic energy, and it is the major (if not the only) source of SEs at medium and high energies; it is normally described as a three-stage process:

1. production of SEs within the sample
2. migration to the sample surface
3. escape through the SEB.

## Kinetic Ion-Induced SE Emission

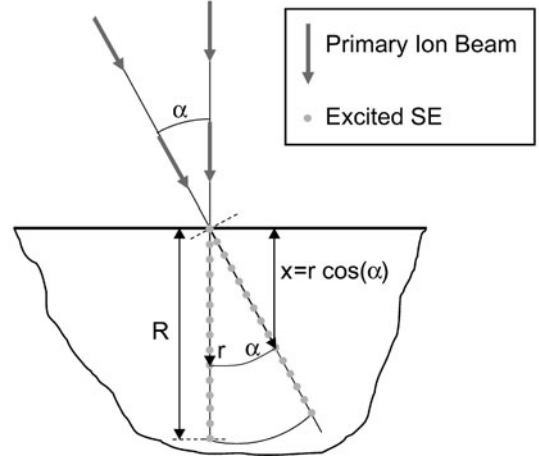


**Figure 1.** The simple origin of the secant law for ion-electron-induced SE emission: the higher the incidence angle, the closer the energized electrons are to the sample surface.

The mechanism of ion-induced kinetic emission is very similar to the electron-induced SE emission; the main difference is in the production stage, while the other parameters (energy-loss rate, mean free path, magnitude and shape of the surface barrier) are common for both cases. In particular, since at a given primary energy the velocity of ions is two or three orders of magnitude lower than for electrons, the electron-induced SE yield ( $\delta_e$ ) exhibits a maximum for energies below 1 keV, while the maximum of the iSE yield  $\delta_i$  is at hundreds of keV. As a result, at the normal operating energies (tens of keV),  $\delta_e$  decreases with increasing primary energy, while the opposite happens for  $\delta_i$ .

The theory of iSE emission is quite well established, and several studies can be found in literature accounting for the variation of  $\delta_i$  with the primary energy and molecular weights of primary ions and target atoms, and for the differences with eSE (Giannuzzi et al., 2008; Griffin & Joy, 2008). The object of the present study, however, is the dependence of  $\delta_i$  on the angle  $\alpha$  formed by the ion beam and the normal to the sample surface, which is at the basis of contrast in scanning ion images. This dependence is less well studied, but a good treatment for  $\delta_i = f(\alpha)$ , can be found in Ferron et al. (1981) or in Svensson et al. (1981). The traditional fitting function for  $\delta_i = f(\alpha)$  is the simple “inverse cosine law” (Sternglass, 1957):

$$\delta_i(\theta) = \delta_i(0) \cos^{-1} \theta. \quad (1)$$

This law accounts only for the second step of the kinetic emission mechanism and can be easily explained with reference to Figure 1; for the incidence angle  $\alpha$ ,  $\delta_i$  can be written as

$$\delta_i(\alpha) = K \frac{1}{\int_0^R r \cos(\alpha) dr}, \quad (2)$$

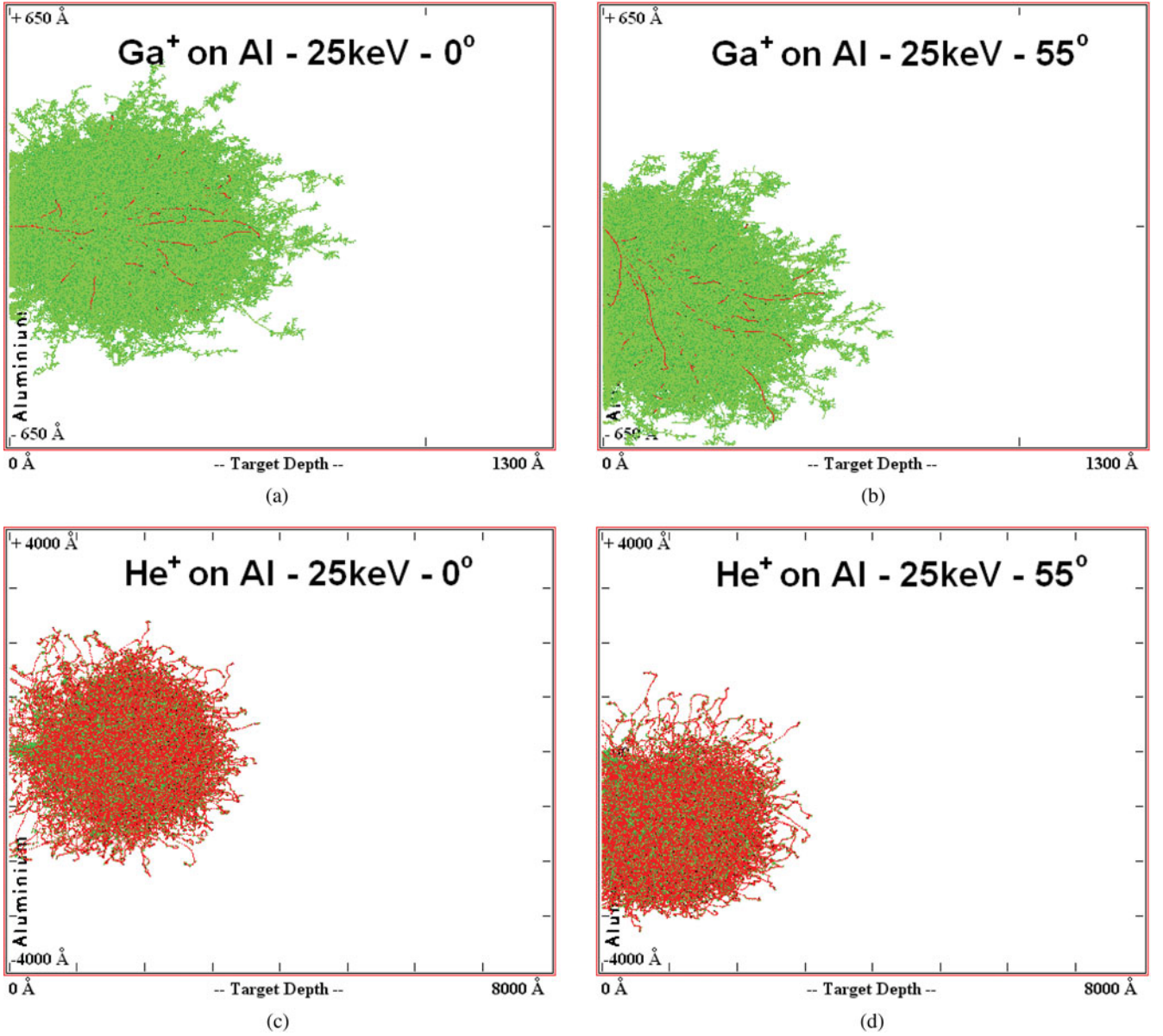


**Figure 2.** Interaction volume: the position inside the sample occupied by primary ions and recoiled atoms for different ions and different incidence angles; the ion beam enters the sample from the left, the impact point being at the center of the vertical axis; (a) Ga<sup>+</sup> on Al, 30 keV and 55°, depth axis: 130 nm; (b) Ga<sup>+</sup> on Al, 30 keV and 55°, depth axis: 130 nm; (c) He<sup>+</sup> on Al, 25 keV and 0°, depth axis: 800 nm; (d) He<sup>+</sup> on Al, 25 keV and 55°, depth axis: 800 nm. The darker points are primary ions; the lighter points are recoiled target atoms.

where  $R$  is the distance inside the bulk material at which ions stop producing electrons and  $K$  is a constant; for  $\alpha = 0$  equation (2) becomes

$$\delta_i(0) = K \frac{1}{\int_0^R r dr}; \quad (3)$$

equation (1) follows directly. A more general expression for  $\delta_i$  can be found in Ferron et al. (1981):

$$\delta_i(x) = C \int_0^R N(r) \exp(-x/L) dr, \quad (4)$$

where  $x$  is the coordinate normal to the sample surface,  $r$  is the linear coordinate along the ion path,  $N(r)$  is the number of electrons produced at  $r$ ,  $L$  is the mean electron attenuation length,  $C$  is a target/dependent constant; equation (1) is obtained for  $N$  constant over distances much larger than  $L$  and a straight ion path [in which case  $x = r \cos(\alpha)$ , as in Fig. 1].

The inverse cosine law is of course quite a gross simplification, even when only considering the migration of electrons to the surface, for they are not produced along a straight line into the sample, but in an interaction volume whose shape can be complex (see Fig. 2). In addition, electrons are not only produced by primary ions, but also by recoils, i.e., target atoms that have been displaced. In fact,

some qualitative predictions can be made on the basis of the interaction volume alone. Comparing Figures 2a and 2c, it appears that the He ions have higher penetration power, resulting in lower SE emission at normal incidence; when the incidence angle increases, the intersection between the interaction volume and the sample surface increases substantially; in the case of Ga ions, on the other hand, the extent of such intersection is less dependent on the angle of the beam. Therefore, a higher SE yield range is expected in the case of He; this prediction will be confirmed in the following sections. However, the fact that, as will be shown, in most cases the secant law is quite a good approximation for  $\delta_i = f(\alpha)$  is a pleasant obscure surprise on one hand and on the other hand proves that the kinetic emission is indeed the dominant emission mechanism, and that the process is usually limited by the second stage, i.e., the distance from the surface where SEs are generated.

At low energies ( $< 10$  keV) the behavior of  $\delta_i(\alpha)$  strongly deviates from the one predicted by equation (1) not only because the potential emission becomes more and more important, but also because more and more primary ions are backscattered and/or reflected. Even at energies of tens of keV, deviations have been observed and, based on Monte Carlo simulations in the energy range 100 eV–1 MeV, a modified version of equation (1) has been proposed and is widely used (Ohya & Kawata, 1994):

$$\delta_i(\alpha) = \delta_i(0)\cos^{-f}(\alpha), \quad (5)$$

where the corrector factor  $f$  can assume values smaller or greater than 1:

1. at intermediate energies, the backscattered ions penetrate below the surface before exiting again, thus enhancing excitation of SEs near the surface  $\Rightarrow f > 1$
2. at low energies, ions can just be reflected from the surface, without contributing to the SE formation  $\Rightarrow f < 1$ .

A similar argument can be made for the incidence angle, for any value of the primary energy: SE production is enhanced at intermediate angles, and strongly suppressed at high incidence angles, which once again results in a deviation from the secant law; this effect can be modeled with a correction factor  $f$  that is a function of  $\alpha$ .

A more general fitting function for  $\delta_i = f(\alpha)$  is found in Yamamura et al. (1987):

$$\delta_i(\alpha) = \delta_i(0) \frac{1}{\cos^{-f}(\alpha)} \exp\left[-g\left(\frac{1}{\cos(\alpha)}\right)\right], \quad (6)$$

where  $f$  and  $g$  are the adjustable parameters.

## THE EXPERIMENTAL SETUP

Secondary emission measurements are notoriously difficult for several reasons (Seiler, 1983):

1. *Backscattered particles.* A fraction of the incident ions find their way out of the sample surface as backscattered ions. These ions are partially responsible for the deviation of the SE yield from the secant law, for they can

contribute to the SE emission in different ways: they can be reflected by the sample, especially at very high angles, thus contributing almost nothing to the SE production, or they can travel for a while inside the sample, close to the surface, thus producing a higher-than-normal number of SEs. In any case, for reasons that will be clear soon, the backscatter yield must be known, or at least estimated, to correctly quantify the SE yield.

2. *Different types of SEs.* SEs can be produced directly by incident ions, or by recoiled atoms cascading into the interaction volume. These secondaries of different origin are usually referred to as  $SE_I$  and  $SE_{II}$ , respectively, and treated separately because they are characterized by different spatial and energy distributions (Ishitani & Ohya, 2003). In the present study a third class of SEs must be taken into account, i.e., those secondaries that are not produced in the sample but by the holder/chamber walls, and still reach the detector. Since  $SE_I$  and  $SE_{II}$  are equivalent with respect to the SE yield, their current is not differentiated and is indicated as  $I_{se1}$ . The current coming from electrons produced somewhere else is called  $I_{se2}$ .
3. *Surface status.* The SE yield is strongly dependent on the work function of the sample material and thus on the surface conditions. In general, the control on the surface status of a sample is scarce, which generates strong uncertainties in the measurement of SE yields. In the case of iSE emission, however, the surface status is much less wild because of the cleaning effect of the ion beam.

The iSE yield is defined as the number of SEs emitted per incident ion:

$$\delta_i = \frac{SE}{ion} = \frac{I_{se}}{I_b}, \quad (7)$$

where  $I_{se}$  and  $I_b$  are the SE current and the primary ion current, respectively. These two currents will be measured on a flat sample at different incidence angles to build curves of  $\delta_i(\alpha)$ . In fact, they cannot be measured directly, but they can be estimated measuring the sample current in two conditions, at different values of  $\alpha$ , with reference to Figure 3, and assuming ionic currents flowing from the column to the sample as positive:

1. *Measurement 1.* The sample is positively biased, and the SE detector is switched off, so that all the produced SEs are pulled back toward the sample: the measured current is  $I_1 = I_b - I_{bs} - I_{se2}$ , where  $I_{bs}$  is the current of the backscattered ions leaving the sample, and  $I_{se2}$  is the (negative) current of SEs produced by backscattered ions anywhere in the chamber and hitting the sample.
2. *Measurement 2.* The sample is negatively biased, and the SE detector is on at the maximum voltage, so that all (or most of) the SEs are collected, and the current measured at the sample is  $I_2 = I_b - I_{bs} + I_{se1}$ , with  $I_{se1}$  being the current of SEs from the sample.

If there were no backscattered ions, then  $I_{bs} = I_{se2} = 0$ ; in this case  $I_{se1} = (I_2 - I_1)$ , and  $\delta_i = (I_2 - I_1)/I_1$ . The

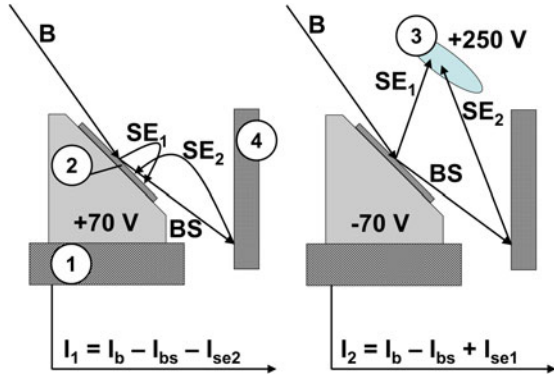


**Figure 3.** A schematic of the setup for the measurement of the iSE Yield  $\delta_i$ . In the first measurement the sample is positively biased and the SE detector is off; in the second measurement the sample is negatively biased and the SE detector is on: 1, sample holder; 2, sample; 3, detector; 4, chamber wall. B are the ions in the primary beam, SE<sub>1</sub> and SE<sub>2</sub> are the SEs emitted from the sample and the chamber walls, respectively, and BS are the backscattered ions.

presence of a nonnegligible backscattered ion current requires a correction, as will be shown later.

The sample bias voltage is set at +70 V in the first measurement, a value that is slightly higher than the highest energy conventionally assumed for the SEs (50 eV), to be sure to pull back all the electrons. In the second measurement the sample bias is set at -70 V to assist the electrons in leaving the surface, without affecting the primary ions, incident at 25–30 keV. It should be noted that the best way to measure the primary current  $I_b$  would be with a Faraday cup, which assures that none of the SEs are lost. The cup, however, should be removed to measure  $I_2$ ; the chamber should be opened at each value of  $\alpha$ , making the whole measurement extremely cumbersome.

In Figure 4 the electric circuit employed for the measurement is shown. Since the sample has to be biased and the current has to be measured at the same time, a floating amplifier, with an optical connection between the input and the output circuit, is used. The impedance of the amplifier is 1 G $\Omega$ , so 1 V in output corresponds to a sample current of 1 nA. The output is measured and recorded via an analog-to-digital card.

Because no stage can be tilted up to  $\pi/2$ , in order to span the whole range of incident angles, two different holders had to be used for each experiment—one flat, tilted up to  $\pi/4$ , and one on which the sample is already at  $\pi/4$ , to allow incident angles up to  $\pi/2$  (see Fig. 3). In machines in which only one sample at a time can be placed, the chamber had to be open and the sample mounted on the tilted stage for measurement at angles higher than  $\pi/4$ .

Considering that the absolute values of the recorded currents always contain an offset (i.e., a nonzero current also when  $I_b = 0$ ),  $I_1$  and  $I_2$  are written as

$$I_1 = I_{off1} + I_b - I_{bs} - I_{se2}, \quad (8)$$

$$I_2 = I_{off2} + I_b - I_{bs} + I_{se1}; \quad (9)$$

The current  $I_{se2}$  only appears in  $I_1$  because in the second measurement these SEs hit the detector, not the sample. The problem is that now the SE current cannot be simply calculated as  $I_{se1} = (I_2 - I_1)$ ; in fact, there is no way to measure the current  $I_{se2}$ , nor to cancel it combining equations (8) and (9). The backscatter yield  $I_{bs}/I_b$  is itself a function of  $\alpha$ , in general monotonically increasing. The minimum value of  $I_{bs}$ , at  $\alpha = 0$ , is usually very close to 0 (see Figs. 7, 10a). Assuming that at normal incidence  $I_{bs}/I_b \approx 0$ , then  $(I_1 - I_{off1})|_{\alpha=0} \approx I_b$ , and  $I_{se1}$  can be approximated in different ways, each characterized by a different error:

- $I_{se1} \approx (I_2 - I_{off2}) = I_{se1} + (I_b - I_{bs})$
- $I_{se1} \approx (I_2 - I_{off2}) - (I_1 - I_{off1}) = I_{se1} + I_{se2}$
- $I_{se1} \approx (I_2 - I_{off2}) - I_b = I_{se1} - I_{bs}$ .

Method b has been dismissed as the most risky, for there is no way to make any assumption about  $I_{se2}$ , which can vary in an unpredictable way, also as a function of the chamber conditions. Methods a and b are roughly equivalent—the first resulting in a slight overestimation, the second in a similarly slight underestimation. For this study, method c is chosen because usually  $I_{bs} < I_b/2$  in most of the angle range  $[0, \pi/2)$ .

## RESULTS I: SECONDARY ELECTRONS FROM $\text{Ga}^+$ BOMBARDMENT

For the experiments on the  $\text{Ga}^+$ -induced secondary emission, a Dual Beam Quanta 3D FEG from FEI (Hillsboro, OR, USA) is used. With a beam current of about 500 pA, the sample is probed in spot mode (i.e., the beam is stationary in a certain position, without scanning) with a focused beam. There are several reasons behind this choice. As expected and observed, the chemical and physical surface changes caused by the ion beam affect the SE production, making  $I_2$  vary in time. In scanning mode, this variation is slow, and  $I_2$  appears to drift in time, so that deciding about its value is rather difficult. In addition, when in the field of view there is a “bad spot,” such as an impurity or a dust particle, the different amount of SEs is mediated over the whole image, getting by totally undetected. The same happens in spot mode with a defocused beam. When working in spot mode with a focused beam, on the other hand, the measured current can be referred to a precise location on the sample, and the spot can be moved several times on the sample, with a fixed step chosen in order not to overlap with the previous position. As can be seen in Figure 5, a graph of  $I_2$  in time appears as a sequence of spikes followed by fast decay (more on this in the Surface Modification subsection below). The maximum of each spike, corresponding to time zero for each new area of illumination, has been taken as the current of interest, for it is the current produced by a “virgin” area of the sample. In this way, given the availability of many measurement points for each measurement, a statistical analysis is possible, allowing the estimation of the error band for each measurement angle. Illumination points in which topological or compositional

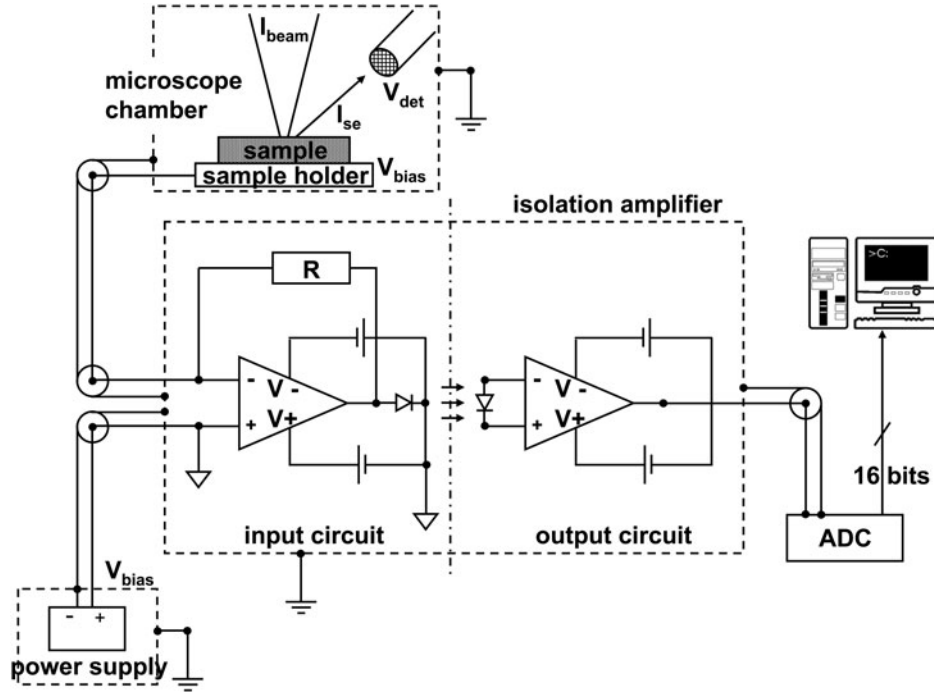


Figure 4. The electronic circuit used for the bias of the sample and the reading and recording of the sample current.

anomalies are present can be recognized easily and dismissed: they give a signal whose magnitude is far off from the magnitude of other spikes in the graph.

Figures 5a and 5c show that also  $I_1$  is a function of time, stronger for higher angles. Also this effect will be discussed in the Surface Modification subsection below. Finally, Figure 5a proves that  $I_{se2}$  is actually present and cannot be neglected at grazing angles (when  $I_{bs}$  is high): it is this term that makes  $(I_1 - I_{off1}) < 0$ . In Figure 6, the curves showing  $\delta_i = f(\alpha)$  for Al and Cr under 30 keV  $\text{Ga}^+$  bombardment, together with the statistical error at each measurement angle.

As has been pointed out already, the value of  $\delta_i$  calculated as  $[(I_2 - I_{off2}) - I_b]/I_b$  is an underestimation, for it is actually  $\delta_i - I_{bs}/I_b$ . These curves therefore should be corrected for the backscatter current  $I_{bs}$ . This can be estimated from  $I_1$ , once the relationship between  $I_{bs}$  and  $I_{se2}$  is assumed. Choosing a simple relationship such as  $I_{se2} = nI_{bs}$ , equation (8) becomes

$$I_1 - I_{off1} = I_b - I_{bs} - nI_{bs} = I_b - (n+1)I_{bs}, \quad (10)$$

where  $n$  is a fraction of the  $\delta_i$  of the chamber walls (not all the backscattered ions hit the chamber, and not all the SE2 are pulled toward the sample). Thus, it is reasonable to assume for  $n$  values of at most few units; the backscatter current can be expressed as

$$I_{bs} = \frac{I_b - (I_1 - I_{off1})}{n+1}. \quad (11)$$

Another way to estimate  $I_{bs}$  is via Monte Carlo simulation, with codes like TRIM (Ziegler et al., 1985). Figure 7 shows the curves of  $I_{bs}/I_b$  versus  $\alpha$  obtained for different values of

the factor  $n$  in equation (11), and as obtained by TRIM simulation, for Al (Fig. 7a) and for Cr (Fig. 7b). Some considerations: first of all, the curves that show values higher than 1 have no physical meaning, for  $I_{bs}$  cannot be greater than  $I_b$ , so that certain values for  $n$  can be dismissed; the values obtained by simulation match in the case of Cr (for  $n = 1$ ) reasonably well up to  $\alpha \sim 0.45\pi$ , but substantially differ in the case of Al (simulations have been also performed covering the Al sample with a 3–5 nm layer of  $\text{Al}_2\text{O}_3$ , for no appreciable difference). With an estimation of  $I_{bs}$  at hand, the curves of Figure 6 can be corrected, simply adding the term  $I_{bs}/I_b$ :

$$\delta_i^{corr} = \delta_i + I_{bs}/I_b. \quad (12)$$

The result is shown in Figure 8, for Al (Fig. 8a) and Cr (Fig. 8b), together with the secant law normalized at  $\delta_i(\alpha = 0)$ . Good news: not even in the worst allowed case (lowest value of the factor  $n$  that keeps  $I_{bs}/I_b < 1$ ) does the correction move the curve outside the error band.

## RESULTS II: SECONDARY ELECTRONS FROM $\text{He}^+$ BOMBARDMENT

For the experiments on the  $\text{He}^+$ -induced secondary emission, a He-microscope ORION from Zeiss (Peabody, MA, USA; www.smt.zeiss.com) has been used. In this case biasing the target has not been possible because it is not well insulated: any voltage applied on it results in a current measured at the sample. While measurement 2 should not be affected much, also because the detector can be biased up to 500 V, the absence of a positive bias in measurement 1 could lead to an overestimate of the beam current  $I_b$ , due to the fact that some SEs might not be reabsorbed into the

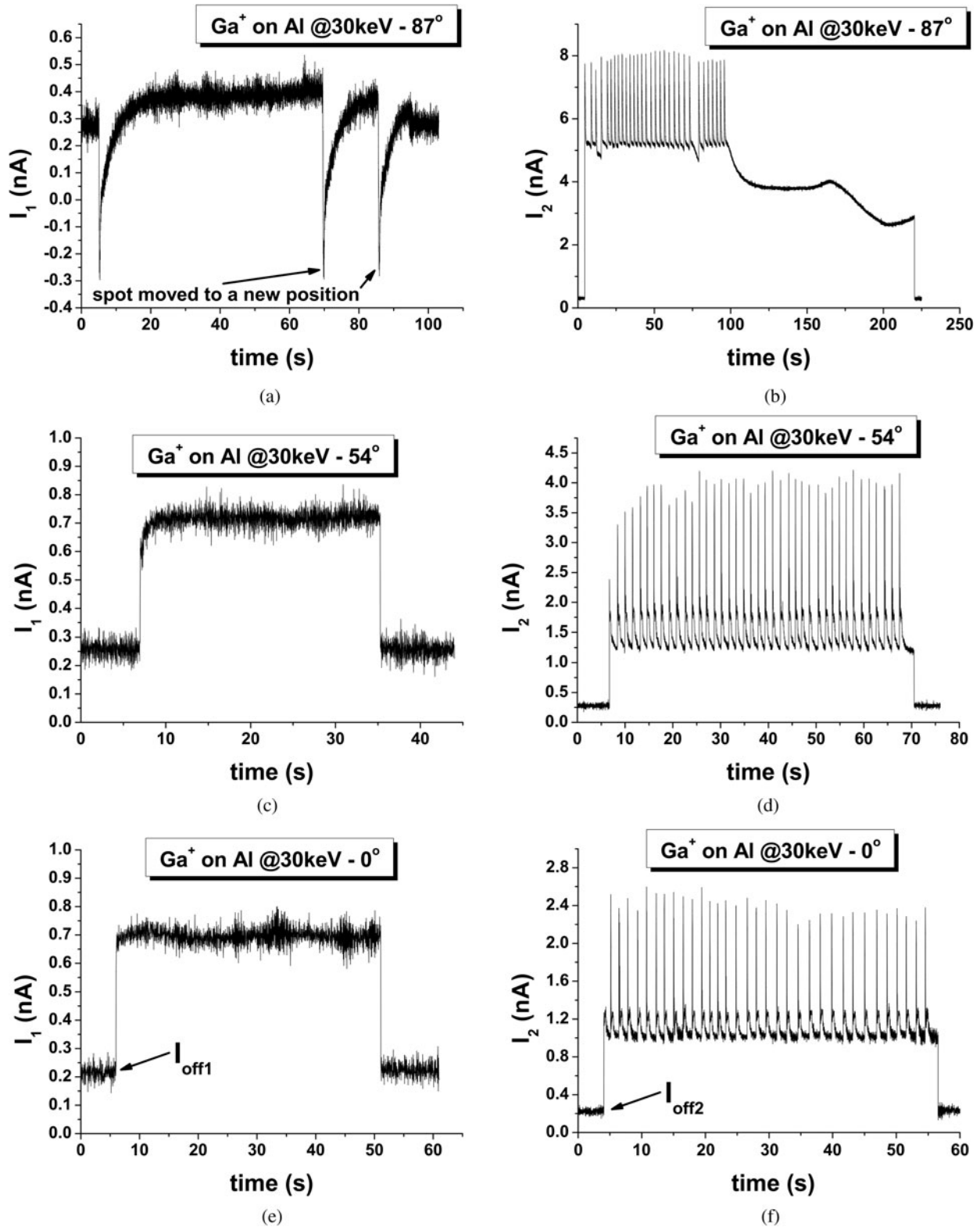
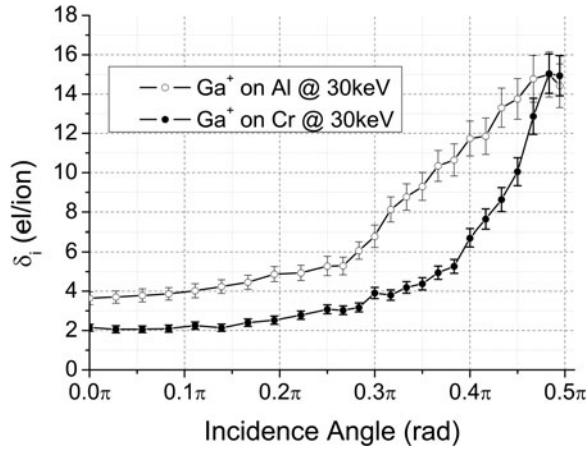


Figure 5. Graphs of the recorded currents  $I_1$  and  $I_2$  for  $\text{Ga}^+$  at 30 keV on Al, for three different incidence angles.

target, thus subtracting a negative current from  $I_1$ . For this reason measurement 1 has not been performed, and  $I_b$  has been taken as the blanker current, as given by the instrument reading. In this case, however, there can still be an overestimation, for all the ions that reach the blanker might

not reach the sample. However, a correction can be performed also in this case, thanks to simulations obtained with the Monte Carlo based code IONiSE, developed by D. Joy (Ramachandra et al., 2009). While there is no commercially/publicly available code that can simulate elec-



**Figure 6.** The experimental curves showing  $\delta_i$  versus  $\alpha$  for Al and Cr under bombardment of  $\text{Ga}^+$  at 30 keV.

tron emission induced by any ionic species (at least none known to the authors), IONiSE is able to produce He-induced SE yields at varying beam energy, incident angle, and target material, once the correct values for the two parameters (Bethe-Salow parameters, see Sternglass, 1957)  $\lambda$  and  $\epsilon$  are selected. In the present study the focus is on Al and Cr targets, whose Bethe-Salow parameters are shown in Table 1. To take into account the likely overestimation of  $I_b$ , the experimental curves can be corrected under the assumption that the real  $I_b$  is only a fraction of the measured one:  $I_b^{real} = xI_b^{meas}$  with  $x \in [0,1]$ ; the coefficient  $x$  is then regarded as a fitting parameter, its value being obtained matching experimental and simulated curves. The experimentally obtained  $\delta_i$  curves, both “raw” and corrected, are shown together with the ones obtained via simulations in Figure 9. The coefficient  $x$  appears to be 0.7 for both target

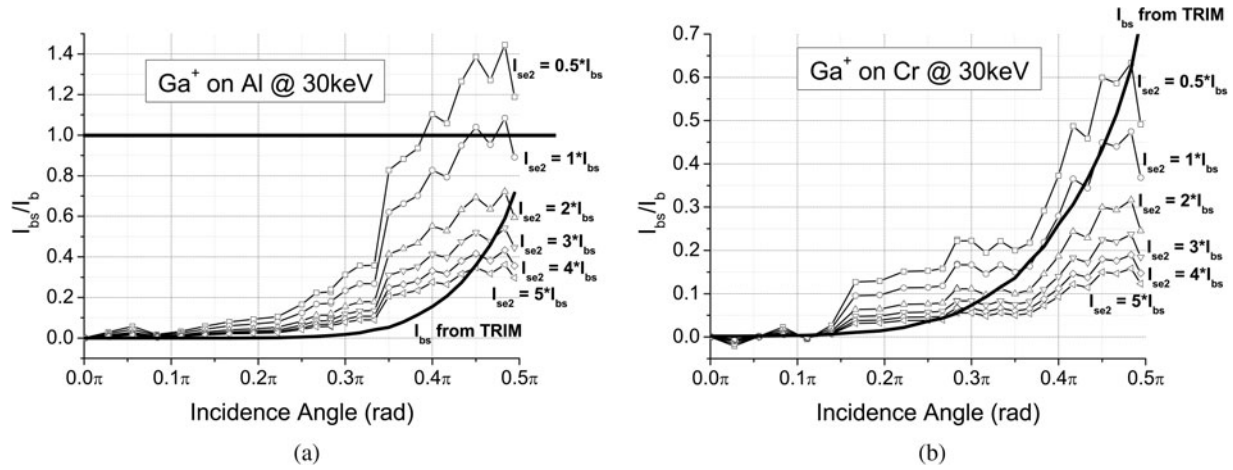


**Figure 7.** Estimation of the backscattered current, as obtained by TRIM simulation and as calculated for different values of the parameter  $n$  in equation (11); the curves showing values greater than 1 have no physical meaning.

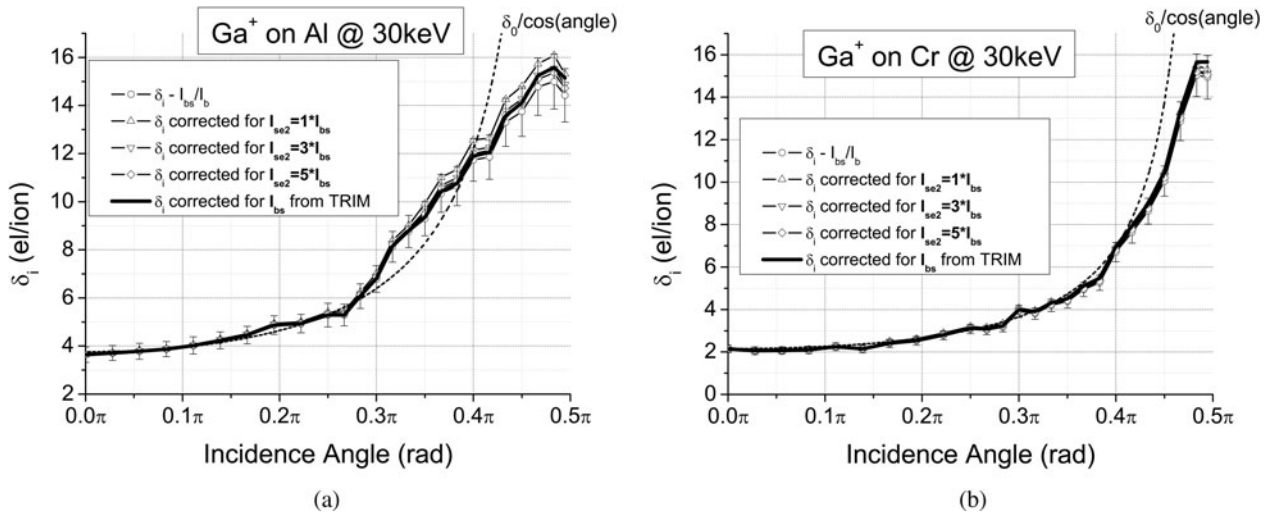


**Figure 8.** Curves of Fig. 6 with different corrections for the backscattered current; in all cases the correction lies within the error band of the original curve. In the graphs, also the secant curve is plotted, for comparison.

**Table 1.** Bethe-Salow Parameters for iSE Emission in Al and Cr.

	$\lambda$ (Å)	$\epsilon$ (eV)
Al	12	40
Cr	7.5	70

materials, i.e., only 70% of the blanker ion current reaches the sample.

As for the Ga-FIB, also in this case the curves of Figure 9 do not take into account the current lost at the target due to the backscattered ions. Also in this case, the fraction of ions that are backscattered can be simulated via TRIM, and  $\delta_i$  can be corrected at each angle with equation (12).  $I_{bs}/I_b$  and  $\delta_i^{corr}$  are shown in Figure 10. It is comforting that even taking into account the backscattered current, the curves do not change drastically.

## DISCUSSION

### Experiments and Simulations

In Figure 9, experimental He-induced SE yield curves together with simulations are shown, for Al and Cr target. In the case of Cr, the two curves match almost in the whole range of incidence angles, differing only above  $0.48\pi$ , while for Al they substantially differ already for angles above  $0.4\pi$ . The most likely explanation for this discrepancy lies in the characteristics of the surface of the samples used for the measurement. Both samples have been made via sputter deposition. As it can be clearly seen in Figure 11a, the Al sample looks very rough at the nanoscale, making it practically impossible for the ion beam to hit the surface at grazing angles: when  $\alpha$  approaches  $\pi/2$  macroscopically, the ion beam hits the surface structures on their side, so that the real incidence angle is always much lower than the apparent one. As a result, the measured value

of  $\delta_i$  at high angles is lower than the value coming from simulations. This effect is much reduced in the case of Cr (but still present) because the surface of the Cr appears to be more regular, as can be seen in Figure 11b. Moreover, it is known that  $\delta_i$  depends as strongly on the surface topology as on the surface composition, and any piece of Al exposed to air becomes swiftly covered with a 3–5 nm thick layer of  $Al_2O_3$ . Further investigation is required to quantify how much the oxide layer influences the SE emission (simulations show, however, that the backscattered yield is not affected by the presence of the oxide layer). For the Ga-induced emission, simulations are not available, but the curves can still be compared with the ideal secant law (see Fig. 8). Once again, Cr behaves “better” than Al: while for the former the curve follows surprisingly well the secant law up to values of  $\alpha$  higher than  $0.4\pi$ , for the latter the curve appears to deviate from the secant law already for  $\alpha \sim 0.25\pi$ . The explanation for this anomaly is beyond the purpose of this study, but it is clear that the secant law is not always a good approximation for  $\delta_i$  also at medium/high energies.

One more thing to point out is that both the Al and Cr samples used in this study are polycrystalline at the nanometric scale, i.e., the target material is assumed to be homogeneous and the length of the ion path in the bulk depends only the ion energy (for a given ion/target pair) but not on the incidence angle. If this is not the case and the sample is monocrystalline (or coarsely polycrystalline), there will be some incidence angles that coincide with low index directions inside the lattice. Ions impinging the target under those angles will encounter a reduced resistance and will be able to travel much longer distances into the sample. This results in depressed secondary emission for certain specific incidence angles, depending on the crystal structure of the sample. A discussion on the channeling effect, including its consequences on nanofabrication, can be found in Kempshall et al. (2001).

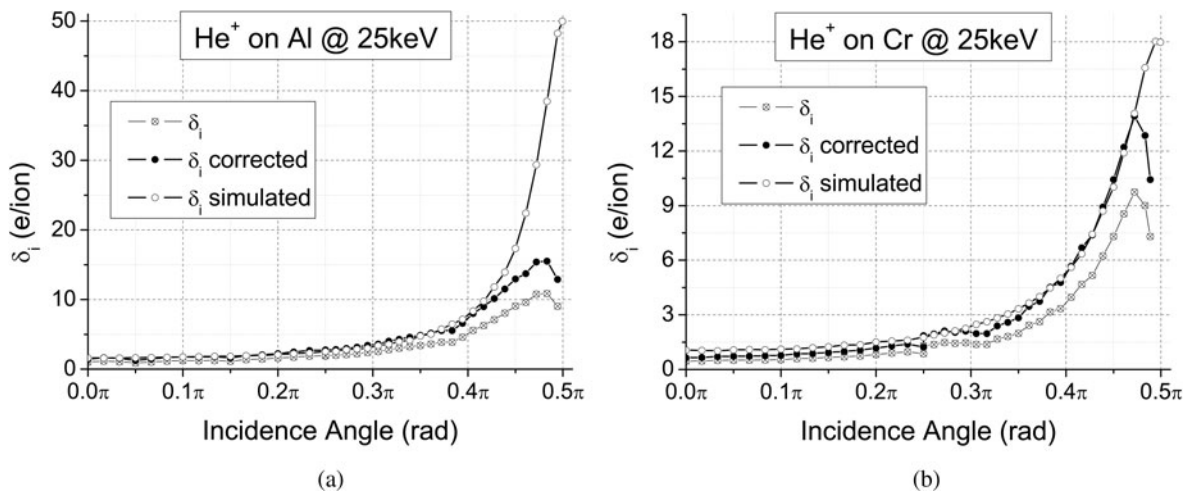


**Figure 9.** Curves of  $\delta_i$  versus  $\alpha$ , for  $He^+$  on Al and Cr at 25 keV, in each graph: the curve as directly obtained by experiment; the curve as obtained by IONiSE simulation; the experimental curve normalized to the simulated values for the first part of the angle range. The discontinuity at  $0.25\pi$  is due to the change of specimen.

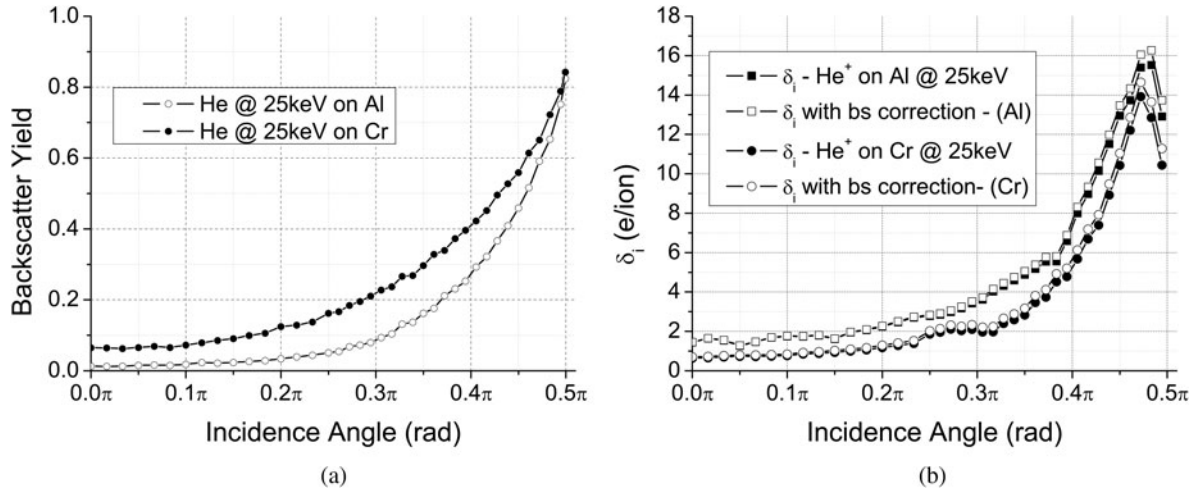


**Figure 10.** (a) Backscatter yields for 25 keV He<sup>+</sup> on Al and Cr, and (b) SE yields corrected for the backscattered ion current.

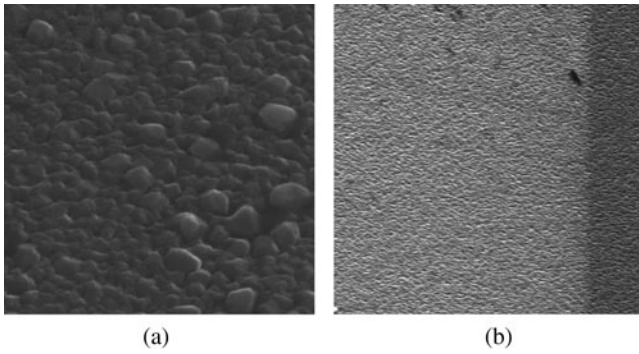


**Figure 11.** (a) SEM image of the Al sample and (b) He image of the Cr sample; both images are taken with the sample tilted at 45°, with a field of view of 2  $\mu$ m.

### SE Yield and Image Contrast

The curves  $\delta_i = f(\alpha)$  can be regarded as the first order term for the contrast mechanism in scanning microscopy, while higher orders come from less local effects that might enhance or suppress the escape of electrons from the sample surface. Figures 12c and 12d show the contrast obtained applying the experimental yield curves to the sample in Figures 12a and 12b. Figures 12e and 12f show line intensity profiles through diameters of the features, and it appears that He ions produce, for both materials, thinner edges when compared with Ga imaging. Also, the features are brighter in the He images, when related to the background level, while the material contrast is, in this case, higher in the Ga images than in the He images. In terms of the yield curves, the reason is that, although the maximum values are impressively close in all cases ( $\sim 15$  electrons per ion at grazing angles), the range is higher for He:  $\delta_{i-max}/\delta_{i-min} \sim 16$ , while the values for Ga<sup>+</sup> are between 5 and 8 (see Table 2). This can be easily explained in terms of interaction volume, as shown in Figure 2. For Ga<sup>+</sup> the interaction volume is much more isotropic, with the consequence that the area of its intersection with the sample surface changes

less with the incidence angle; for He<sup>+</sup>, on the other hand, a normal incident beam produces many fewer electrons that are close enough to the sample surface to be emitted as SEs. Incidentally, this also means that the information carried by each pixel in a Ga image refers to a similar area around the impact point at every point of the image, while in a He image the information coming from a steep point is, so to say, less local.

### Surface Modification

Figure 13 shows details of the graphs  $I_2$  versus time in Figure 5, recorded for  $\sim 600$  pA of Ga<sup>+</sup> current in a focused spot on Al. Two things are striking here; first, the SE signal drops very fast to just a fraction of its maximum at the time zero of each new beam position; second, the shape of the peaks seems very repeatable at each  $\alpha$ . The reason of the signal drop must be connected with the surface modification that the sample surface undergoes under ion bombardment. In particular, it could be either due to sample contamination/charging (it is known in scanning microscopy that an area becomes darker when imaged over and over again) or to surface sputtering/redeposition: if a hole is dug, fewer electrons make it out of the sample, and the deeper the hole, the fewer electrons escape. A full understanding of this phenomenon certainly requires further investigation, but the fact that the signal dynamics appears to be exactly the same at each incidence angle gives the latter explanation more credibility, for if it was due to charging/

**Table 2.**  $\delta_i^0$ ,  $\delta_i^{max}$ , and Their Ratio for the Different Pairs Ion/Atom Analyzed in This Study.

	$\delta_i^0$	$\delta_i^{max}$	$\delta_i^{max}/\delta_i^0$
Ga/Al	3.6	16	4.45
Ga/Cr	2	15.5	7.75
He/Al	1.4	16.3	11.65
He/Cr	0.7	14.7	21

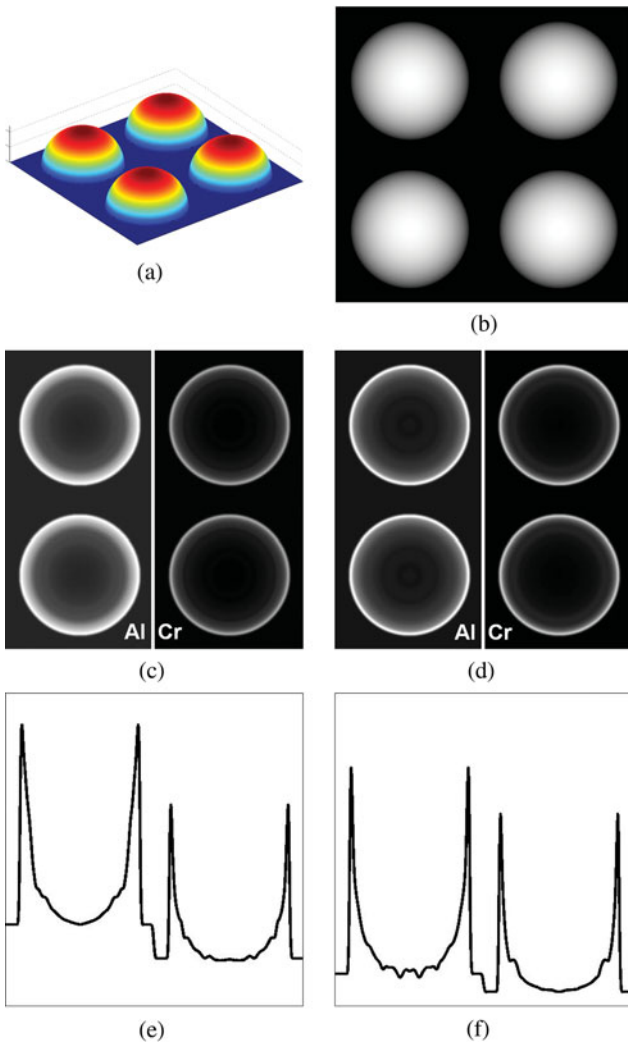


**Figure 12.** First order material and topological contrast: sample, visualized (a) as a three-dimensional plot of the surface and (b) as height map; (c) contrast from 30 keV  $\text{Ga}^+$ ; (d) contrast from 25 keV  $\text{He}^+$ ; (e, f) line intensity profiles through diameters of the features in the pictures above; the zero of the intensity axis is at the bottom line; the units are arbitrary.

contamination, the variation would have been much less regular. Holes are indeed dug during the measurement, as can be seen from a SEM image of an area of the Al sample subjected to ion beam irradiation during the measurement shown in Figure 14. Similar arguments can be made to explain the time dependence of the current  $I_1$  at high angles, evident from Figures 5e, 5c, and 5a. At low angles  $I_1 \approx I_{se1} \approx 0$ , so that  $I_1 \approx I_b$ , constant in time. When the angle increases, more ions are backscattered, and more SEs are produced by these ions hitting the chamber walls, thus reducing  $I_1$ . With a beam standing still on the sample, however, and a hole dug on the sample surface, backscattered ions can enter again into the sample, so that the deeper the hole, the fewer backscattered are lost, and the fewer SE2 are produced. In time,  $I_1$  tends to approach the value of  $I_b$ . Comparing Figures 5a and 5b, it appears that the variation of  $I_1$  and  $I_2$  is characterized by a different

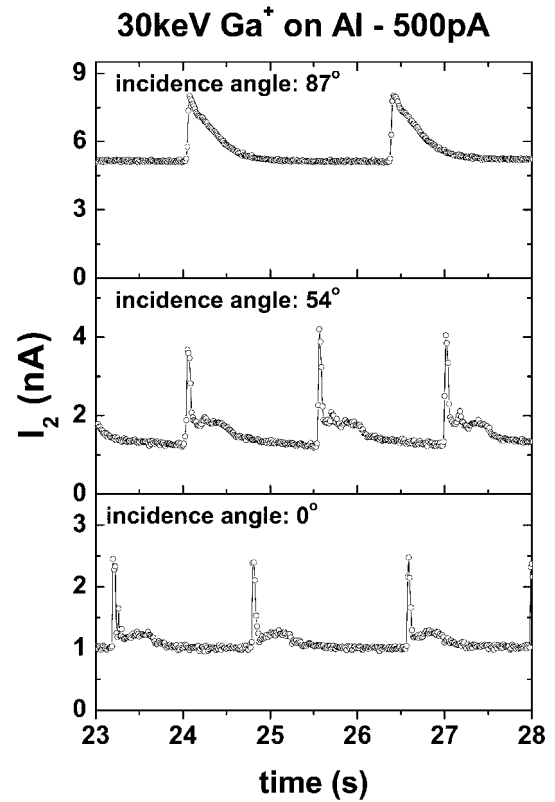


**Figure 13.** Details of the graphs  $I_2$  versus time in Figure 5, showing that the current dynamics of the sample after ion bombardment to a new spot are repeatable for each incidence angle.

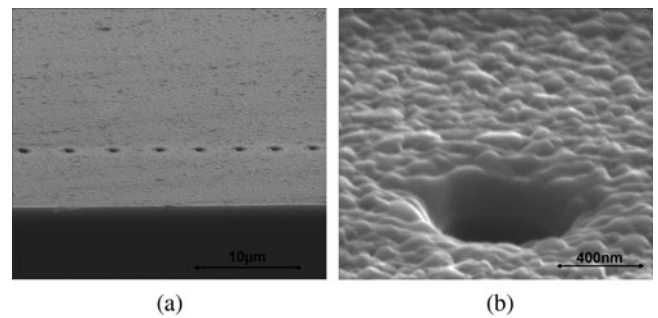


**Figure 14.** SEM micrographs showing the surface modification on the Al sample due to Ga ions; each spot results from few seconds of irradiation with  $\sim 500$  pA in a focused beam; the field of view is (a)  $30 \mu\text{m}$  and (b)  $1.5 \mu\text{m}$ .

time constant,  $I_2$  varying much faster. The reason for this could be the fact that, on average, backscattered ions have higher energy than SEs: they can escape from deeper holes.

The connection between time dynamics of  $I_{se1}$  and sputtering of the sample is also suggested by the plots in Figures 15 and 16. Figure 15 is taken for a  $\text{He}^+$  current of  $\sim 200$  pA and shows a constant current over the whole angle range. Figure 16 is taken for a higher current,  $\sim 600$  pA: in this case the current signals begins decaying in time for high values of  $\alpha$ , showing that surface modification is taking place. Figure 17 compares the current signals at high incidence angle generated from a focused  $\text{He}^+$  beam and

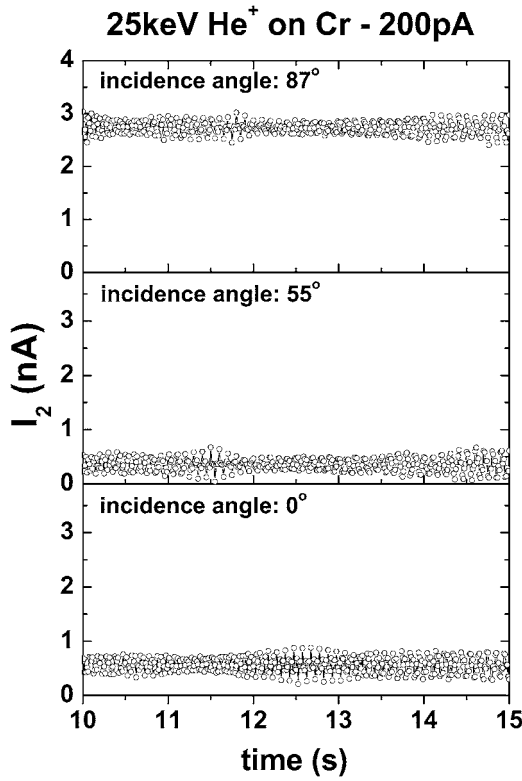


Figure 15. Current  $I_2$  versus time for 25 keV  $\text{He}^+$ , with a focused spot of  $\approx 200$  pA. The current is constant at all values of the angle  $\alpha$ .

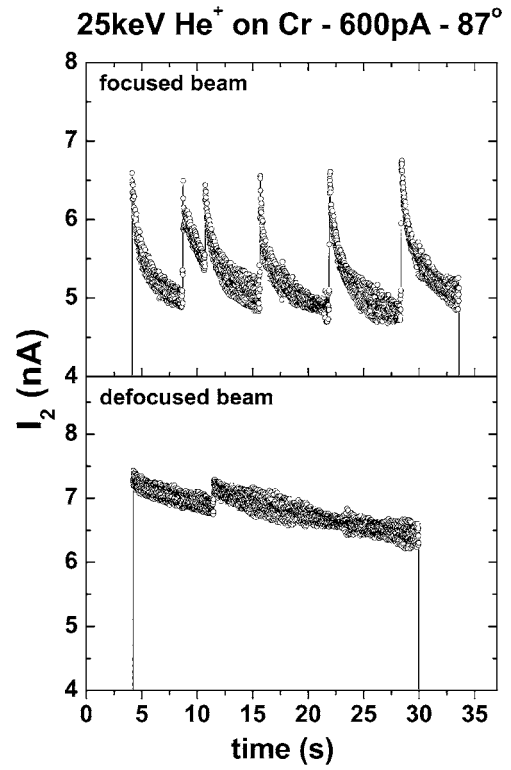


Figure 17. Different dynamics recorded for  $I_2$  when probing the sample with a focused and a slightly defocused ion beam.

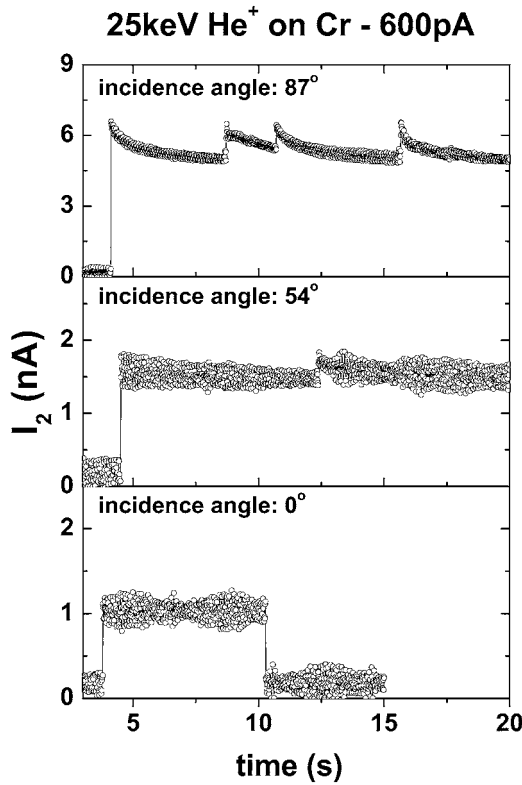


Figure 16. Current  $I_2$  versus time for 25 keV  $\text{He}^+$ , with a focused spot of  $\sim 600$  pA. The current shows similar dynamics as in Figure 13, but smaller in magnitude and only for high  $\alpha$ .

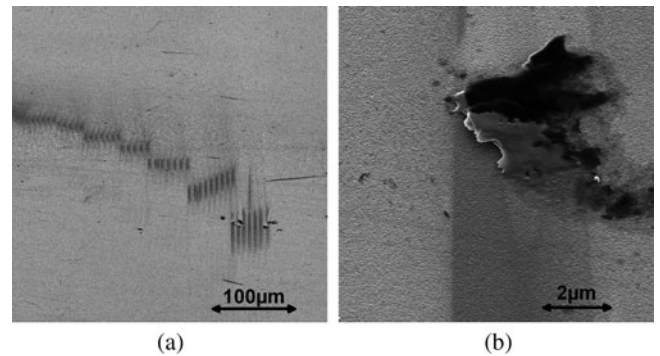


Figure 18. He micrographs showing the surface modification on the Cr sample due to He ions. Each spot results from a few seconds of irradiation with  $\sim 600$  pA in a focused beam. The field of view is (a)  $400 \mu\text{m}$  and (b)  $10 \mu\text{m}$ .

from a slightly defocused one. In the first case, after the same exposure time, the ion dose received by the sample is much higher, resulting in a more profound surface modification; this is in turn reflected in a higher variation of the current signal in time. Figure 18 shows the footprints of the  $\text{He}^+$  beam on the Cr sample. In Figure 18a different sets of marks, showing that  $\delta_i$  has dropped, are visible, the more elliptic ones coming from higher incidence angles. Figure 18b shows a spot in which a dust particle is present, on which Cr atoms appear to have been redeposited.

The fact that the signal dynamics at each new spot is repeatable for each incidence angle has a twofold implication. On the one hand, it is a proof that each spot actually

represents the sample surface, for a different one (like a particle of dust) would give a clearly different signal. On the other hand, it shows that the electronic dynamics are uniquely correlated with the topology of the surface. A further analysis of these current recordings could result in a better understanding of the sample modification under ion bombardment.

## CONCLUSIONS

In this article, measurements of the ion-induced secondary electron yield as a function of the ion beam incident angle have been performed for different pairs of ion/atom.

Several factors that influence the results have been analyzed: modification of the sample surface under ion bombardment, backscattered ions, production of SEs from places other than the sample. The influence of each of these factors has been discussed and, in the case of the backscattered ions, quantified.

The resulting curves have been compared with the secant law (Ga-induced emission) or with simulations (He-induced emission). In both cases the Cr appears tamer than Al: the match is good up to  $0.4\pi$  for Ga/Cr, and up to  $0.48\pi$  for He/Cr; but only up to  $0.25\pi$  for Ga/Al, and up to  $0.4\pi$  for Ga/Cr.

The maximum value of  $\delta_i$  is very similar in all cases ( $\sim 14$ – $16$  electrons/ion), but the SE yield range for He is higher than for Ga, due to the lower He-induced SE emission at low angles. This translates in a better topographic contrast for the He microscope.

## ACKNOWLEDGMENTS

This work is part of the research program “Microscopy and Modification of Nano-structures with Focused Electron and Ion Beams” (MMN) of the “Stichting voor Fundamenteel Onderzoek der Materie” (FOM), which is financially supported by the “Nederlandse Organisatie voor Wetenschappelijk Onderzoek” (NWO). The MMN program is cofinanced by FEI Company. The authors also wish to thank David Joy for his kind support with the code IONiSE and for providing the values of the Bathe-Salow parameters.

## REFERENCES

- BELL, D. (2009). Contrast mechanisms and image formation in helium ion microscopy. *Microsc Microanal* **15**, 147–153.
- CASTALDO, V., HAGEN, C.W., KRUIT, P., VAN VELDHoven, E. & MAAS, D. (2009). On the influence of the sputtering in determining the resolution of a scanning ion microscope. *J Vac Sci Technol B* **27**(6), 3196–3202.
- CASTALDO, V., HAGEN, C.W., RIEGER, B. & KRUIT, P. (2008). Sputtering limits versus signal-to-noise limits in the observation of Sn-balls in a  $\text{Ga}^+$  microscope. *J Vac Sci Technol B* **26**(6), 2107–2115.
- FERRON, J., ALONSO, E., BARAGIOLA, R. & OLIVA-FLORIO, A. (1981). Dependence of ion-electron emission from clean metals on the incidence angle of the projectile. *Phys Rev B* **24**(8), 4412–4419.
- GIANNUZZI, L.A., UTLAUT, M. & SCHEINFELD, M. (2008). Relative contrast in ion and electron induced secondary electron images. *Microsc Microanal* **14**(S2), 1188–1189 (CD-ROM).
- GRIFFIN, B.J. & JOY, D. (2008). Variation of Rutherford backscattered ion and ion-induced secondary electron yield with atomic number in the “Orion” scanning helium ion microscope. *Microsc Microanal* **14**(S2), 1190–1191 (CD-ROM).
- HAGSTRUM, H.D. (1954a). Auger ejection of electrons from tungsten by noble gas ions. *Phys Rev* **96**(2), 325–335.
- HAGSTRUM, H.D. (1954b). Theory of Auger ejection of electrons from metals by ions. *Phys Rev* **96**(2), 336–365.
- HILL, R., NOTTE, J. & WARD, B. (2008). The ALIS He ion source and its application to high resolution microscopy. *Physics Procedia* **1**, 135–141.
- ISHITANI, T. & OHYA, K. (2003). Comparison in spatial spreads of secondary electron information between scanning ion and scanning electron microscopy. *Scanning* **25**(4), 201–209.
- KEMPSHALL, B.W., SCHWARZ, S.M., PRENITZER, B.I., GIANNUZZI, L.A., IRWIN, R.B. & STEVIE, F.A. (2001). Ion channeling effects on the focused ion beam milling of Cu. *J Vac Sci Technol B* **19**(3), 749–754.
- OGAWA, S., THOMPSON, W., STERN, L., SCIPIONI, L., NOTTE, J., FARKAS, L. & BARRISS, L. (2010). Helium ion secondary electron mode microscopy for interconnect material imaging. *Jpn J Appl Phys* **49**(4), 04DB12.
- OHYA, K. & ISHITANI, T. (2003). Comparative study of depth and lateral distributions of electron excitation between scanning ion and scanning electron microscopes. *J Electron Microsc* **52**(3), 291–298.
- OHYA, K. & KAWATA, J. (1994). Monte Carlo study of incident-angle dependence of ion-induced kinetic electron emission from solids. *Nucl Instrum Meth B* **90**(1–4), 552–555.
- ORLOFF, J. (1993). High-resolution focused ion beams. *Rev Sci Instrum* **64**(5), 1105–1130.
- ORLOFF, J., SWANSON, L.W. & UTLAUT, M. (1996). Fundamental limits to imaging resolution for focused ion beams. *J Vac Sci Technol B* **14**(6), 3759–3763.
- ORLOFF, J., UTLAUT, M. & SWANSON, L.W. (2003). *High Resolution Focused Ion Beams*. Boston, MA: Kluwer Academic/Plenum Publishers.
- RAMACHANDRA, R., GRIFFIN, B. & JOY, D. (2009). A model of secondary electron imaging in the helium ion scanning microscope. *Ultramicroscopy* **109**(6), 748–757.
- SEILER, H. (1983). Secondary electron emission in the scanning electron microscope. *J Appl Phys* **54**(11), R1–R18.
- SELIGER, R.L., WARD, J.W., WANG, V. & KUBENA, R.L. (1979). A high-intensity scanning ion probe with submicrometer spot size. *Appl Phys Lett* **34**(5), 310–312.
- STERNGLASS, E. (1957). Theory of secondary electron emission by high-speed ions. *Phys Rev* **108**(1), 1–12.
- SVENSSON, B., HOLMEN, G. & BUREN, A.A. (1981). Angular dependence of the ion-induced secondary-electron yield from solids. *Phys Rev B* **24**(7), 3749–3755.
- TONDARE, V.N. (2005). Quest for high brightness, monochromatic noble gas ion sources. *J Vac Sci Technol A* **23**(6), 1498–1508.
- WARD, B., NOTTE, J.A. & ECONOMOU, N.P. (2006). Helium ion microscope: A new tool for nanoscale microscopy and metrology. *J Vac Sci Technol B* **24**(6), 2871–2874.
- YAMAMURA, Y., MOSSNER, C. & OECHSNER, H. (1987). The bombarding-angle dependence of sputtering yields under various surface conditions. *Radiat Effects* **103**, 25–43.
- ZIEGLER, J.F., BERSACK, J.P. & LITTMARK, U. (1985). *The Stopping and Range of Ions in Solids*. New York: Pergamon Press (1996 revised Ed.). Information for SRIM and TRIM available at [www.srim.org](http://www.srim.org) (the TRIM code is available for free download).